ELSEVIER

Journal of Power Sources 110 (2002) 364–376

JOURNAL OF POWER SOURCES

www.elsevier.com/locate/jpowsour

Computational battery dynamics (CBD)—electrochemical/thermal coupled modeling and multi-scale modeling

C.Y. Wang*, Venkat Srinivasan

Electrochemical Engine Center, Department of Mechanical and Nuclear Engineering, Pennsylvania State University, University Park, PA 16802, USA

Abstract

This paper reviews the development of first-principles based mathematical models for batteries developed on a framework parallel to computation fluid dynamics (CFD), herein termed computational battery dynamics (CBD). This general-purpose framework makes use of the similarity in the equations governing different battery systems, and has resulted in the development of robust models in a relatively short time. Here we review this framework, in the context of applications to the coupled modeling of the thermal and electrochemical behavior of cells, and to the modeling at three different scales, namely pore-level, cell-level and stack-level. The similarity and differences of our approach with other research groups are exemplified. Significant results from each of these advanced applications of modeling are highlighted with emphasis on the insights that can be gained from a first-principles model. In addition, we also demonstrate the usefulness of a combined experimental-modeling approach in describing cells. The models reviewed here are expected to be useful in predicting the behavior of advanced batteries used in electric vehicles (EVs) and hybrid electric vehicles (HEVs).

Keywords: Computational battery dynamics; Multi-scale phenomena; Thermal behavior; Direct numerical simulation; Stack simulation

1. Introduction

The recent interest in the development of environmentally friendly vehicles powered either fully (electric vehicles, EVs) or partially (hybrid electric vehicles, HEVs) by batteries has resulted in enhanced research into various aspects of this electrochemical energy source. These range from the development of better designs to suit the application (e.g. designs favoring high power for HEVs while favoring high energy for EVs) to the development of new materials with superior performance. Parallel to various experimental research programs, mathematical models that describe the behavior of batteries and their interaction with other devices in a vehicle have also received much attention. These models range from those that describe the physics of the various phenomena in the cell (first-principles models [1]) to ones that are fit to experimental data under various conditions (equivalent circuit [2] and neural network models [3]).

While models that are trained to experimental data provide great benefit in their ability to fit into vehicle models with ease, due to their simple construction and fast computational speed, they possess many shortcomings. Specifically, the models are only as good as the experimental data they are trained to, and thereby do not provide the ability to extrapolate beyond the range of this data. In addition, changes in design of the cell do not permit the use of the same models, and the task of building prototype cells, collecting data and training the model has to be repeated. More importantly, as these models are empirical in nature, they provide little, if any, insight into the working of the cell. These disadvantages are offset by the use of first-principles models, however at a price of more computational demand and added complexity. Therefore, it would be advantageous to develop models that combine the strengths of these two classes. With this in mind, our goal is to develop models based on the physics that would (i) provide insight into the operation and limiting mechanisms; (ii) allow for changes in design (iii) predict behavior of cells under wide range of operating conditions, like rates and temperatures; (iv) perform these operations with great speed; (v) allow for visualization tools and user friendly interfaces and (vi) allow for integration into vehicle models. These six goals can be achieved by adapting the knowledge base developed over the last three decades in the fluid flow field with the use of computation fluid dynamics (CFD) to the field of batteries (i.e. computational battery dynamics, CBD).

CBD can be thought to encompass four key components, namely (i) physicochemical model development,

* Corresponding author. Tel.: +1-814-863-4762; fax: +1-814-863-4848.
E-mail address: cxw31@psu.edu (C.Y. Wang).

0378-7753/02/$ – see front matter
PII: S0378-7753(02)00199-4

Nomenclature

a_{sj}	interfacial surface area per unit volume (cm^2/cm^3)
A	area for heat transfer (cm^2)
c_{avg}	average concentration of spherical particle $= (1/2F)\int_0^t i(t)\,dt(4\pi R_s^2/(4/3)\pi R_s^3)$ (mol/cm^3)
c_e	concentration of the electrolyte (mol/cm^3)
c_s	surface concentration in spherical particle (mol/cm^3)
c_{max}	maximum concentration (mol/cm^3)
C_p	specific heat (J/kg K)
D	diffusion coefficient (cm^2/s)
F	Faraday's constant (96487 C/eq.)
h	equivalent convective heat transfer coefficient (W/cm^2 K)
i_{nj}	transfer current density (A/cm^2)
$i(t)$	current density (A/cm^2)
I_0	initial current density (A/cm^2)
k	rate of change of current (A/cm^2 s)
l_s	diffusion length (cm)
q	volumetric heat generation rate (J/cm^3 s)
R_s	radius of the spherical particle (cm)
t	time (s)
T	temperature (K)
U_j	equilibrium potential (V)
V_c	cell volume (cm^3)
V_{cell}	cell voltage (V)

Greek letters

κ^{eff}	effective solution conductivity (Ω^{-1} cm^{-1})
λ	thermal conductivity (W/cm K)
ρ	density (kg/cm^3)
σ^{eff}	effective matrix conductivity (Ω^{-1} cm^{-1})
ϕ_s	potential in the matrix phase (V)
ϕ_e	potential in the solution phase (V)

Subscripts

avg	average over cell
amb	ambient

(ii) advanced numerical algorithms, (iii) material and property characterization and (iv) model validation, all of which are illustrated in this paper. This approach has proved to be very useful in the generation of new models for various batteries [4–10] and even for fuel cell systems [11] in a short time. In other words, the general framework on which CBD is based, and the similar equations that are used to describe these different systems, has allowed us to use the knowledge gained in developing one battery model in the other, hence minimizing the learning curve considerably. In addition, graphical user-interfaces have been used to make the models user friendly. These models have also been linked to Simulink and have been successful in predicting the behavior of EV batteries under DST and SFUDS tests and compare to experimental data adequately [12].

In this paper, we illustrate CBD by reviewing the development of a multi-scale model for battery systems, which incorporates a pore-level model [13], a cell-level model [4–10] and finally a stack model [14]. The cell model developed here is a coupled thermal–electrochemical model that not only predicts the electrochemical behavior but also the thermal excursions in the cell and associated changes in electrochemistry. We first review the development of the general-purpose model framework that solves the coupled thermal–electrochemical problem for various batteries. The physics included in the model and the subtleties/approximations incorporated for the development of macro-homogeneous cell models are detailed. In addition, the use of this framework in the development of pore-level models using a direct numerical simulation (DNS) technique is shown, after which the solution of these problems using a general-purpose solver incorporating advanced solution algorithms is detailed. Subsequently, we illustrate the cell-level models using the Li-ion cell and Ni–MH cell as examples, where our combined model/experimental approach is illustrated. We then move to pore-level models and show the usefulness of the DNS technique. Finally, the behavior of two Ni–H_2 cells connected in parallel is shown, to illustrate our ability to simulate stack behavior. Work is underway to combine all three-scale models into a single tool, which can then be used to design advanced batteries at various levels of interest, e.g. porous electrodes with optimized pore structures, single cells with certain energy and power capabilities, and stacks for vehicular applications with desirable combinations of safety, performance, and life.

2. Mathematical model development

2.1. Macro-homogeneous electrochemical cell model

As mentioned in Section 1, the models developed in this paper are based on first-principles and incorporate the physics of the various processes occurring in the cell. Fig. 1 illustrates the battery modeled in this study, which consists of a positive electrode (e.g. nickel hydroxide or lithium manganese oxide spinel), a negative electrode (e.g. metal-hydride or carbon) and a separator with the whole cell filled with electrolyte (e.g. 33% KOH in Ni–MH cells). The active material may be pasted onto a porous grid, as in a Ni–MH cell or on a planar current collector, as in a Li-ion cells. The electrodes represented in the figure can be thought of as half the actual electrode thickness, with equivalent processes occurring in the other half. Symmetry enables us to neglect the processes in the other half. All three sections consist of at least two phases, metal and solution with a gas phase in some battery systems due to the presence of overcharge gassing reaction (e.g. oxygen evolution in the nickel electrode). The porous nature of the electrodes results in added ohmic and diffusion resistances due to the tortuous ionic and electronic pathway. In addition, the existence of two different phases

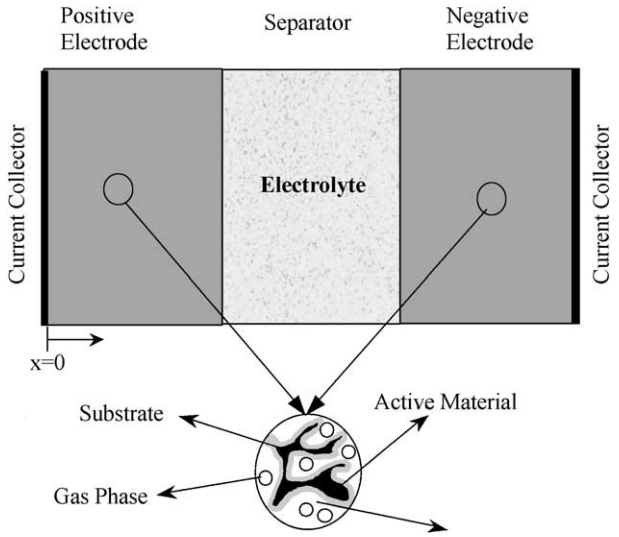

Fig. 1. Schematic of the cell that is described in the cell-level models, which consists of two porous electrodes with a separator between them. The whole cell is filled with electrolyte. Consequently, each control volume consists of matrix, solution and in some cases a gas phase. The active material shown in the inset consists of many particles attached together, one of which is simulated in Fig. 2.

results in the need to keep track of the volume fraction and the surface area of each phase, which could change during charge/discharge, due to changes in the partial molar volume of the materials. This is achieved by using a macro-homogeneous approach where the detailed geometry of the pore is ignored. The porosity and the surface area are averaged over a control volume in the porous electrode using either a porous electrode approach [1,15–17] or a volume averaging approach [9,18,19] and subsequently used to correct the various balances in the cell. For an extensive review of flooded porous electrode models, see De Levie [20], Posey [21] and Newman and Tiedmann [22]. For more details on the subsequent developments in porous electrode theory, see Weidner [23] and Wang et al. [9].

While porous electrode theory accounts for mass transfer, ohmic drops and reaction in a volume element, many battery electrodes may involve additional processes. These could include solid phase diffusion, liquid phase diffusion in pores, precipitation and subsequent film formation. For example, in the Li-ion cell, solid phase diffusion of lithium in the active material can be rate limiting under certain conditions, hence requiring models to describe this phenomenon. This introduces an additional length scale into the problem, which requires a separate treatment. If the particles are considered to be spherical, then the diffusion equation needs to be solved in spherical coordinates at every volume element, in addition to solving for transport in the x-direction in the porous electrode. This can be accounted for using a pseudo two-dimensional approach [24–29], or by numerically integrating the time-dependent boundary condition [30–32]. Owing to the computational tediousness of the former, the latter has been preferred in the literature. One such example was illustrated by Doyle et al. [32] where the authors numerically solve for the solid phase diffusion using the Duhamel's superposition integral and incorporate this into their porous electrode model.

Although the exact solution method [30–32] provides considerable improvement in speed compared to the pseudo two-dimensional approach, it is limited to restrictive assumptions (e.g. perfectly spherical particles and constant diffusion coefficient in the solid phase, where the exact integral solution is possible). In addition, it results in an additional numerical step at each control volume, hence consuming CPU time. As flexibility and speed are important criteria for our models, we use the diffusion length concept, developed by Wang et al. [9] where the surface and average concentration is assumed to be linearly related via a diffusion length. Mathematically this can be expressed as [9]

$$c_s(t) = c_{avg}(t) + \frac{i(t)l_s}{nFD} \tag{1}$$

where the diffusion length, l_s, is related to the dimensions of the particle and depends on the morphology [9]. For example, in spherical particles this is given by $R_s/5$. The term $i(t)$ represents the current density that changes with time. This can be thought of as the reaction current in a porous electrode, which changes with state-of-charge. Although Eq. (1) is physically intuitive and computationally simplistic, the assumption that the surface and average concentrations are linearly dependent on each other is valid only after the diffusion layer builds up to its steady state value. This can be clearly seen in Fig. 2, where the dimensionless surface minus the average concentration is plotted with dimensionless time in a spherical particle, where the reaction current is linearly decreasing with time with slope k (i.e. $i(t) = I_0 - kt$). As expected, the concentration reaches a steady state value as soon as the current is switched on, after which it decreases linearly with time, mirroring the decrease in the current. Also plotted is the exact solution obtained using the Duhamel's integral method [33], which shows that the concentration starts at zero and reaches the steady state value after a time constant, suggesting that the results obtained using Eq. (1) would be inadequate at short times or under dynamic operation (like pulse or current interrupt).

Considering the exponential increase in the concentration at short times, which reaches an asymptotic value, Eq. (1) can be empirically corrected in order to obtain a better match to the Duhamel's solution. An intuitively expressed correction of the form

$$c_s(t) = c_{avg}(t) + \frac{i(t)l_s}{nFD}[1 - e^{-4\sqrt{Dt}/3l_s}] \tag{2}$$

which incorporates another time-dependent term in an exponent similar to the time constant for diffusion, with a multiplier 4/3, has been seen to provide good results under a wide range of operating conditions. Surprisingly, it was shown by comparing with the exact solution that the multiplier 4/3 was valid under all three geometries (planar,

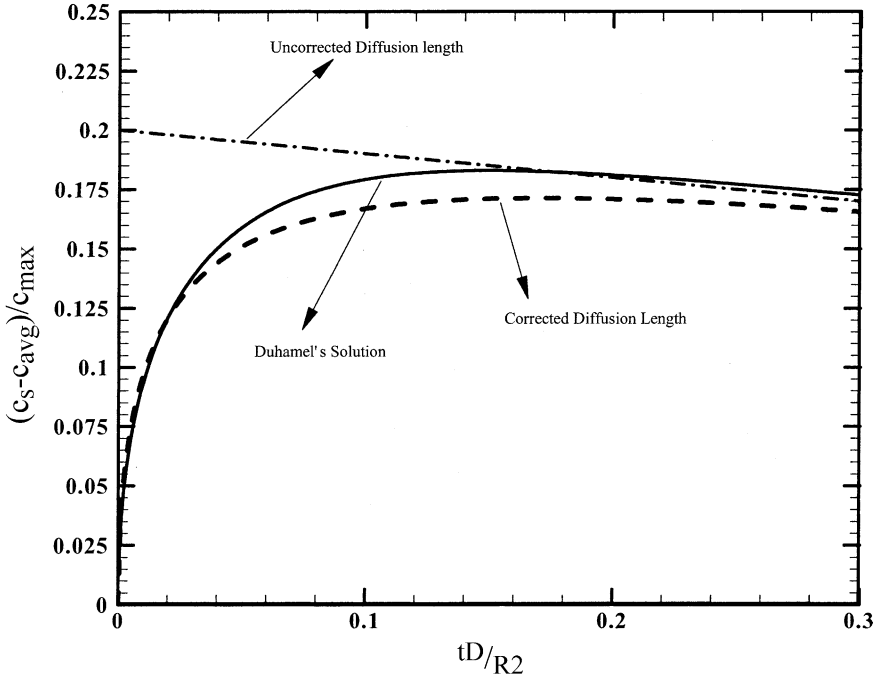

Fig. 2. Dimensionless concentration vs. dimensionless time simulated for a spherical particle with symmetry at the center and a flux at the surface decreasing linearly as $(I_0 - kt)/nF$. Generated for $(I_0 R_s/nFDc_{max}) = 1$ and $(kR_s^2/nFD^2c_{max}) = 0.5$. The average concentration is obtained using faradays law by integrating the decreasing current over time. The plot shows the Duhamels solution (solid line) and comparisons with Eq. (1) (dash-dotted line) and (2) (dashed line).

cylindrical and spherical). Fig. 2 also shows the prediction from Eq. (2) where the adequate fit to the Duhamel's solution is clear. Eq. (2) provides a simple analytical method of adequately describing the diffusion in the solid phase with no added complexity. However, caution needs to be exercised and results verified, preferably with exact analytical or numerical solutions, before application to a system with new particle morphologies.

While the above describes the method used to track the species surface concentration, the potential is estimated based on the thermodynamics and kinetics of the system. In addition, the reaction at the electrode surface results in changes in concentration and generation of current, which are then tracked using charge balance and mass balance equations. As typical cells contain high concentrations of ions (e.g. 33% KOH is used in Ni–MH cells) concentrated solution theory is used for this purpose where in addition to accounting for non-idealities, the interaction of the solute with each other is taken into account [34–37]. Charge balance is accounted for using Ohms law, which is modified when used in the solution phase, in order to account for the diffusion potential.

2.2. Coupled thermal–electrochemical model

Incorporation of the above phenomena results in the simulation of the cell electrochemistry with predictions of the concentration, SOC, reaction current and phase potentials profiles across the cell in addition to cell voltage and current. In order to generate a thermal model, these equations are coupled with an energy balance at each control volume, given by [8,38]

$$\frac{\partial(\rho C_p T)}{\partial t} = \nabla(\lambda \nabla T) + q \tag{3}$$

which accounts for heat accumulation, conduction and generation. Assuming a binary electrolyte and neglecting the enthalpy of mixing and phase change effects, the heat generation term can be estimated based on the various losses in the cell, and expressed as [6,8,38]

$$q = \sum_j a_{sj} i_{nj} (\phi_s - \phi_e - U_j) + \sum_j a_{sj} i_{nj} T \frac{\partial U_j}{\partial T} + \sigma^{eff} \nabla\phi_s \nabla\phi_s + \kappa^{eff} \nabla\phi_e \nabla\phi_e + \kappa_D^{eff} \nabla \ln c_e \nabla\phi_e \tag{4}$$

where the summation is over all reactions. The first term on the right represents the deviation of the potential in each control volume from the equilibrium potential (irreversible heat). The second term arises from the entropic effects (reversible heat) [39]. In intercalation electrodes, the reversible heat can be used to gain insight into the insertion mechanism and gauge the nature of the insertion sites [41]. Note that the first two terms can be rewritten as the deviation of the cell potential from the enthalpy potential or thermoneutral potential of each reaction [40]. Summation of the two terms accounts for the irreversible and reversible heats associated with each electrochemical reaction. The third term represents the ohmic heat arising from the matrix phase, while the last two terms arise from ohmic heats in the solution phase. Note that all the terms that are needed in

Eq. (4) are predicted using an electrochemical model, hence allowing us to simulate the thermal–electrochemical behavior of the cell. However, as the temperature of the cell changes, the various controlling parameters in the cell, like diffusion coefficients and conductivities, change. These are estimated based on Arrhenius-type relations or from measured correlations. Note that Eqs. (3) and (4) represent the local heat generation method and result in the estimation of the temperature at every point in the cell. When the cell temperature is uniform everywhere (small Biot number) one can replace this by a lumped thermal analysis [8,38,42]. Here, the energy balance integral, given by

$$\frac{\mathrm{d}(\rho_{\mathrm{avg}} C_{p,\mathrm{avg}} T_{\mathrm{avg}})}{\mathrm{d}t} + \frac{hA(T_{\mathrm{avg}} - T_{\mathrm{amb}})}{V_{\mathrm{c}}} = \langle q \rangle \tag{5}$$

is used to describe the whole cell, with a heat generation term obtained by integrating Eq. (4) over the whole cell to yield

$$\langle q \rangle = \frac{1}{V_{\mathrm{c}}} \int_{V_{\mathrm{c}}} q \, \mathrm{d}v \tag{6}$$

Only under the condition that the reaction distribution is uniform across the porous electrode, and when no side reactions are present, Eq. (6) is reduced to the expression derived by Bernardi et al. [42].

$$\langle q \rangle = I \left[U_{\mathrm{avg}} - V_{\mathrm{cell}} - T_{\mathrm{avg}} \frac{\partial U_{\mathrm{avg}}}{\partial T_{\mathrm{avg}}} \right] \tag{7}$$

Therefore, either Eq. (5) is solved with Eq. (6), wherein the temperature variation in the cell is neglected, or Eq. (5) is solved with Eq. (7), whereby the non-uniform reaction distribution is also neglected. While the Ni–MH model neglects the temperature variation, whereby Eqs. (5) and (6) are solved [8], the Li-ion model employs the local heat generation method using Eqs. (3) and (4) [6].

2.3. Pore-level model and direct numerical simulation

Some battery systems, like the Li-ion cell, have only 5–10 particles across the thickness in each electrode [43,44]. Under these conditions, the averaging of the various quantities described in the porous electrode approach starts to break down. Therefore, a new kind of modeling framework is needed for such systems. In addition, as macro-homogeneous models neglect the detailed morphology of the microscopic electrode/electrolyte interface a study of these microscopic effects will help in the development of better descriptions of cell behavior and allow for interfacial engineering of porous electrodes. While a number of models exist that solve for solution phase potentials and concentrations in idealized pore geometries [20,45,46], no first-principle model for the current and concentration distributions in both the matrix and solution phases of a porous electrode exists. With this in mind, the DNS approach, traditionally used in modeling turbulence flow in fluid mechanics and combustion in porous media [47], has been incorporated into the framework of CBD [13].

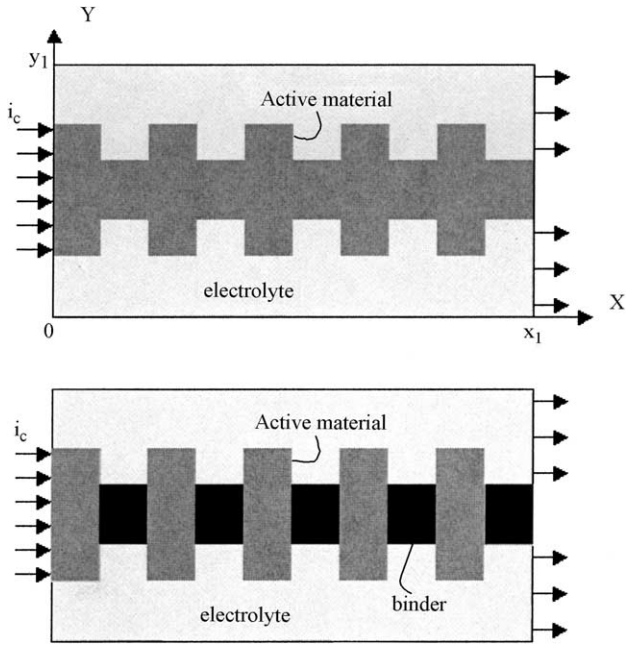

Fig. 3. Schematic of the active material configuration simulated in the pore-level models using DNS. Model 1 (top) consists of a continuous sawed active material, while model 2 (bottom) has a non-reactive conductive matrix which separates the active material. The current collector is located to the left and the separator to the right.

Consider an idealized geometry, as shown in Fig. 3, consisting of matrix and solution phases in the carbon electrode of a Li-ion cell. The geometry is divided into a number of computational cells that consist of either the matrix or the solution phase. This is different from porous electrode theory, where each control volume has both matrix and solution in it. Charge and mass balance expressions are written for each control volume, which remains the same irrespective of whether it describes the matrix or solution, with only the material properties varying in each phase. At the control volumes bordering the metal–solution interface, reaction occurs, which is accounted for using Butler–Volmer kinetics. The resulting equations, when solved, provide the concentration and potential distributions in each phase across the electrode with time. This approach provides us the flexibility of directly simulating complex morphologies of porous electrodes.

Two different configurations are illustrated, (i) consisting of a continuous sawed carbon electrode (Fig. 3a) and (ii) the electrode in (i) is split with a conductive but non-reactive binder (Fig. 3b) [13]. The electrodes are immersed in a solution of 2:1 EC:DMC. Fig. 3 is assumed to be representative of one section of the porous electrode shown in Fig. 1, with repeating units making up the whole electrode. Hence symmetry is assumed to be valid at the top and bottom of the modeled unit system. The right end of the figure represents the separator, which is assumed to be at a constant concentration (assumed to be the initial concentration). All model properties are based on Doyle et al. [43].

3. Model solution

The electrochemical transport phenomena, when mathematically described, result in a set of coupled non-linear partial differential equations, which can be cast into a general form of the convective-diffusion equation

$$\frac{\partial \Phi}{\partial t} + \nabla(v\Phi) = \nabla(\Gamma \nabla \Phi) + S \tag{8}$$

where Φ is the general-purpose variable (e.g. concentration, potential), Γ the diffusion coefficient, v the velocity and S is the source term that incorporates all terms that do not fit into the other three terms. The equations are then discretized using the finite volume method introduced by Patankar [48], which results in a set of algebraic equations. These equations are either solved iteratively one after the other or simultaneously using a Newton method coupled with a GMRES (generalized minimal residual) solver. The use of these advanced methods results in the simulation of the discharge process of a two-dimensional thermal–electrochemical coupled battery model in approximately 10 min.

4. Illustration of CBD: multi-scale modeling of batteries

4.1. Cell-level model with thermal–electrochemical coupling

We begin by examining the importance of an electrochemical model in predicting the thermal behavior of cells by taking the Li-ion cell as an example. The results shown are for an EV cell with a large height to thickness ratio consisting of a carbon negative and a $LiMn_2O_4$ positive electrode in 2:1 EC:DMC. Most of the cell thermal parameters were taken from Baker and Verbrugge [49], while the thickness of the electrodes and the electrochemical parameters (diffusion coefficients, equilibrium potentials) were taken from Doyle et al. [43]. The temperature dependence of the various parameters (e.g. exchange current densities) were taken from Botte et al. [50]. More details on the parameters used can be found in [6]. The entropic term (see Eq. (4)) has previously been neglected due to lack of data. However, recently reported data for the two electrodes used in this study has permitted us to use this information in the present model. For the manganese oxide spinel, the data present by Thomas et al. [41] was used, while for the carbon electrode the data presented by Al Hallaj et al. [51] as a function of equilibrium potential was used to estimate it as a function of amount of lithium intercalated.

Consider a case when the cell simulated is situated in the middle of a cell stack. Under these circumstances no heat dissipation occurs from the sides of the cell and all dissipation occurs from the top, through the tabs. Fig. 4a, which shows the temperature distribution during a 2 C discharge a 2.9 Ah Li-ion cell at 50% SOC, suggests that the large aspect ratio can lead to significant two-dimensional effects. As the top of the cell is exposed to the ambient, the temperature at the cell top can be considerably lower than at the cell bottom.

This distribution of temperature in the cell results in the reaction current being different at different points in the cell, as seen in Fig. 4b [6]. Note that the separator has zero reaction current as no charge transfer occurs in this region, while the current have different signs in the two electrodes. While even under isothermal conditions changes in the

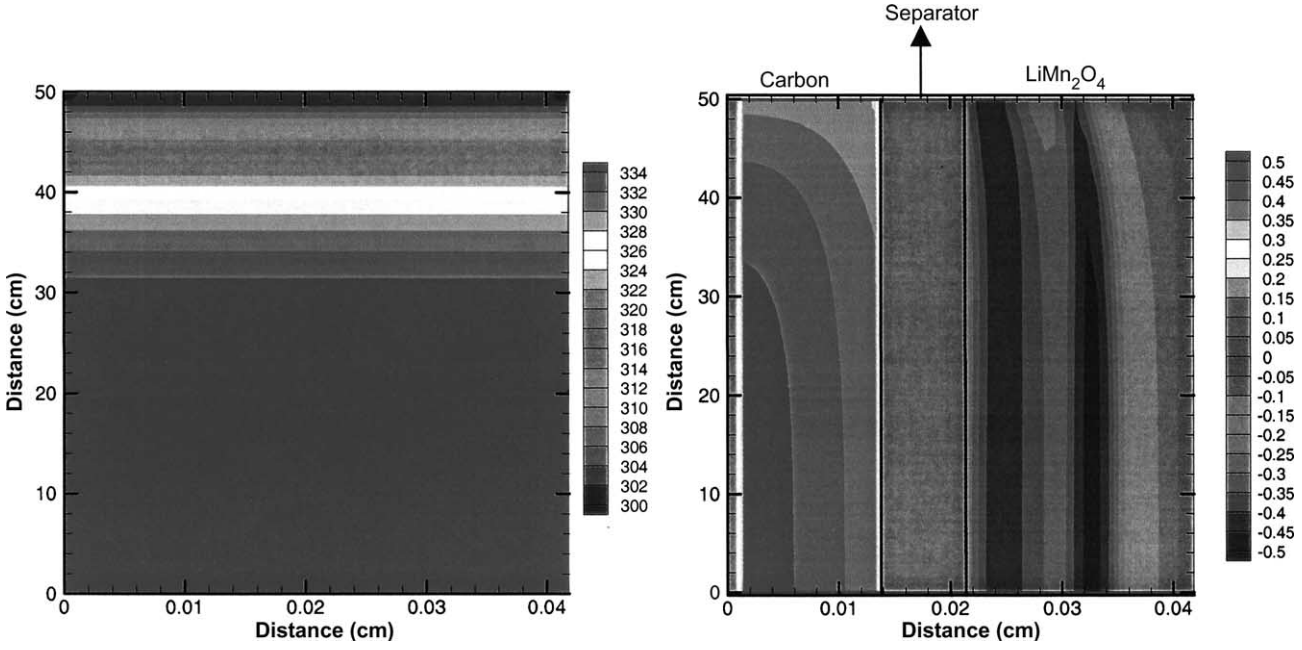

Fig. 4. Temperature (left) in K and reaction current (right) in A/cm^3 contours generated in a Li-ion cell during 2 C discharge at 50% SOC. The features incorporated in the model are detailed in the text. See [6] for more details. Heat dissipation is assumed to occur only from the top of the cell.

reaction current across the porous electrode could occur depending on the ratio of the matrix to solution phase conductivities, the kinetic resistance and the slope of the equilibrium potential with SOC [52], Fig. 4b has the added effect of having different behavior due to differences in temperature. This is seen more clearly in the carbon electrode where the changing reaction current with cell height, especially at the top of the cell, is apparent. Note that the temperature variation seen in Fig. 4a can decrease considerably by decreasing the cell height or by choosing current collectors (which have two orders of magnitude larger thermal conductivity) of larger thickness.

The change in the electrochemical behavior with change in temperature, seen in Fig. 4b, is clearer in Fig. 5 where the cell voltage is plotted at different rates under isothermal and non-isothermal conditions. The non-isothermal case was simulated using infinite heat dissipation from the top of the cell but no heat dissipation from the sides. At low rates (0.01 C) the cell is practically at equilibrium and hence heat generation occurs only due to the reversible heat effects. However, as the time of discharge under these conditions is large, heat dissipation from the cell results in negligible increase in the temperature (not shown) even under the non-isothermal case. As the temperature rise is small, no effect is seen in the electrochemical behavior. However, as the rate increases, the temperature in the cell starts to increase. This increase results in a decrease in the kinetic, mass transfer and ohmic resistances in the cell, which results in the higher voltage at the same SOC. In addition, the increase in the solid phase diffusion results in an increase in the utilization of active materials. For example, during a 2 C discharge, as much as 25% increase in utilization is seen due to the higher temperature. In summary, Figs. 4 and 5 assert that while the thermal behavior of the cell is dictated by the electrochemistry, the electrochemical behavior is considerably affected by the thermal excursions. The coupling of the two gives rise to thermal runaway.

Considering the complexity involved in developing an electrochemical model for cell, it is tempting to avoid this problem by using a lumped thermal model (see Eq. (5)) and estimating the heat generation rate from experimental data instead of Eq. (6) or 7. For example, the heat generation can be estimated by either performing experiments at isothermal conditions and using the difference in the cell potential from the thermo-neutral potential [53], or by performing experiments using an isothermal calorimeter. In other words, this approach assumes that the heat generation under isothermal conditions is same as that under non-isothermal conditions. However, as seen in Fig. 5, as the temperature of the cell increases, the losses in the cell decrease, which in turn will decrease the heat generation rate, hence making this assumption suspect [54].

This can be clearly seen in Fig. 6, where the heat energy from the cell during a complete discharge is plotted with *C*-rate for isothermal and non-isothermal cases. The figure was generated by performing discharge simulations at various rates and integrating the heat versus time curve to calculate the total thermal energy generated. Fig. 6 shows two distinctive features, namely (i) a peak in the energy as the discharge rate is increased and (ii) a significant difference in the energy between the isothermal and non-isothermal cases. At low rates, the cell is operating at equilibrium conditions

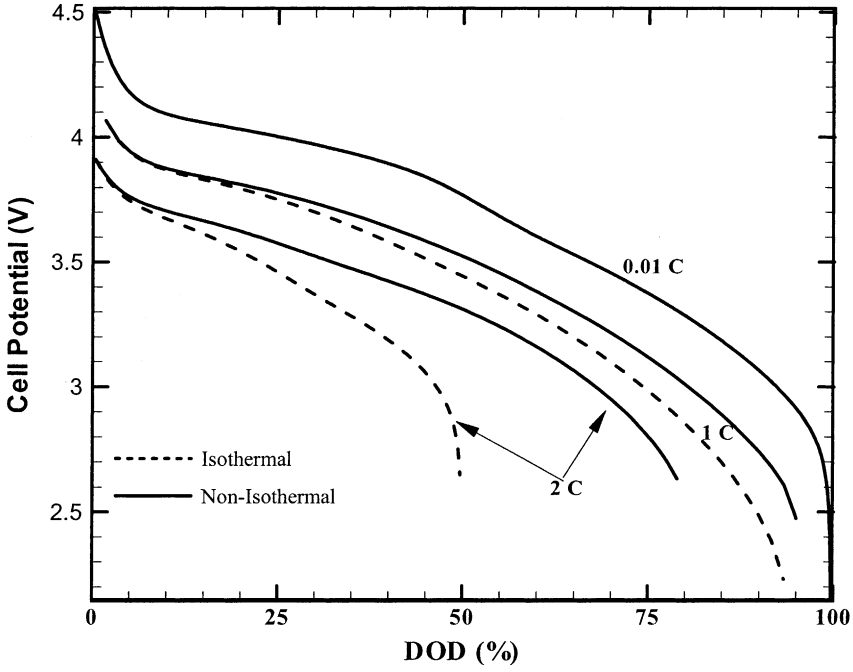

Fig. 5. Voltage vs. DOD at different rates for a Li-ion cell. Graphs are generated under isothermal conditions (dashed line) and when heat dissipation occurs from only the top of the cell (solid line). See [6] for details of the parameters used.

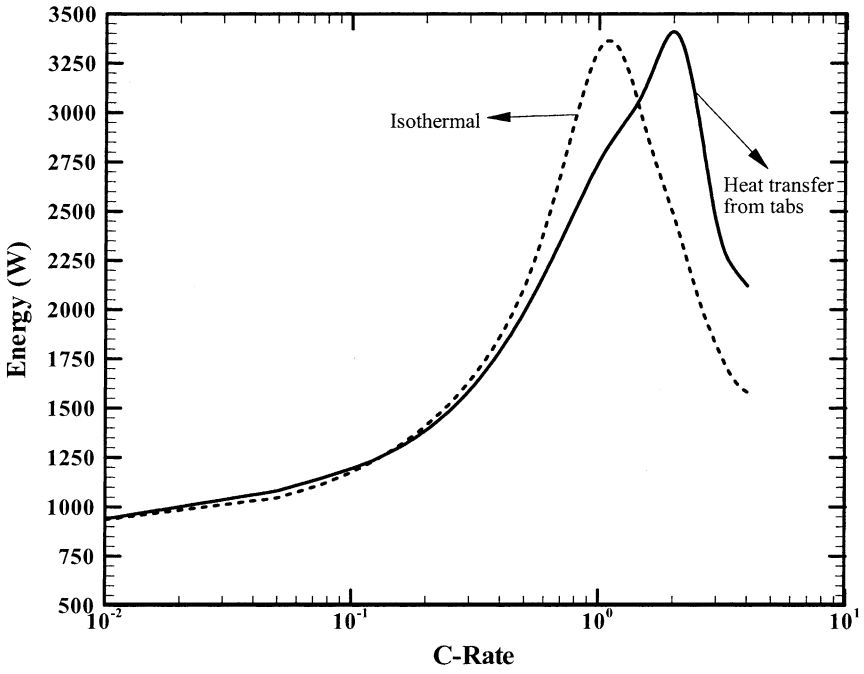

Fig. 6. Energy generated from a Li-ion cell during discharge at different *C*-rates. The graph was obtained by integrating the heat generation curve over the whole discharge. The graph compares the isothermal to the non-isothermal case.

whereby the energy dissipated is due to the entropic heat and hence a constant. As the rate increases, kinetic, ohmic and mass transfer losses start to increase, leading to an increase in the energy. However, at very high rates, although the heat generation is large, the utilization starts to decrease, hence decreasing the time for heat generation. This results in a decrease in the total energy generated, hence, leading to a peak.

Fig. 6 clearly shows that the non-isothermal and isothermal heat generation data are not identical and can vary by as much as 50% from each other, whereby predictions of the temperature of the cell would be inaccurate. In addition, while the temperature would be under-predicted at certain rates, it would be over-predicted in others. It should be noted that curves similar to those shown in Fig. 6 could be generated under different conditions (e.g. natural convection, forced convection, adiabatic) with no two being the same. Therefore, experimental data under any one condition cannot be used to predict thermal behavior under other conditions, asserting the need for a combined thermal–electrochemical modeling approach.

Having established the need for a combined thermal–electrochemical approach, we now turn to examples of property characterization and model validation. This is illustrated for a Ni–MH cell, where model to isothermal experimental comparison was conducted on a commercial 95 Ah, 12 V Ni–MH EV battery. The model, which uses a lumped thermal analysis, includes the side reactions due to oxygen evolution in the nickel electrode and oxygen reduction and hydrogen evolution in the MH electrode [5,8]. Scanning electron microscope images and BET surface area measurements on the two electrodes showed that the particle sizes of the active materials (500 nm in the MH and 50 nm in the Ni electrode) were small enough that solid-state diffusion limitations could be neglected. In addition, the cells were torn down to measure the thickness and porosities of the electrodes and separator, which were then used in the model. Experiments at low rates (*C*/20) were assumed to represent equilibrium conditions and was used to estimate the equilibrium potential as a function of SOC. It was seen that the nature of the curve was very different from a Nemstian or other traditional activity coefficient corrected thermodynamic models [55–57], and hence was fit to an empirical equation.

Experiments were then performed at a rate of 4 C, where the cell showed considerable limitation, although with little loss in capacity at lowered cut-off potentials, asserting to the validity of the assumption that solid phase diffusion was not a limitation mechanism in these cells. With the assumption that the ohmic drops in the porous electrodes and separator were known, the only unknown parameter in the cell is the kinetics. Therefore, the i_0 and α of the Ni electrode were changed in order to obtain a adequate match to the experimental data. Using these values of the kinetic parameters, the model was used to predict the behavior of the cell at other rates, as shown in Fig. 7, where the excellent fit of the model to the data is seen at all four rates, suggesting that the phenomena included in the model were adequate in predicting cell behavior under a wide range of operating conditions.

The advantage of having a mathematical model that predicts the behavior of the cell is the ability to extrapolate to different operating conditions. One example of this is shown in Fig. 8, where the cell voltage versus time is shown

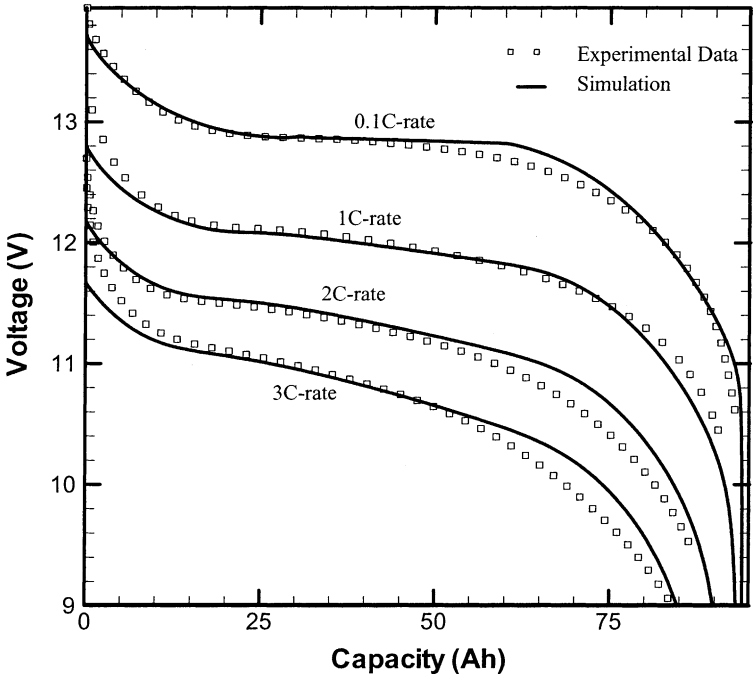

Fig. 7. Experimental vs. model predictions of discharge curves at various rates for a Ni–MH cell. The model was fit to the data generated at 0.05 and 4 C and then used to predict the voltage at the rates shown.

for a 1.2 V Ni–MH cell during constant current charge under different heat transfer coefficients ranging from isothermal to adiabatic conditions. The plot also shows the temperature rise during the charge. As the cell shifts from operating from isothermal to adiabatic conditions, as expected, the temperature of the cell increases. Under adiabatic conditions, temperatures as high as 80 °C are predicted, asserting to the need for thermal management systems in these cells. Notable in Fig. 8 is the voltage rollover seen close to the end of charge, which becomes steeper as the temperature of the cell increases. This rollover feature, which has been seen experimentally, is caused by the oxygen reduction reaction at the MH electrode. As a Ni–MH cell is charged, oxygen evolves from the positive electrode, according to

$$4OH^- \rightarrow O_2 + 2H_2O + 4e^- \quad (9)$$

which is then transported to the negative via the separator. At the negative, the large driving force for the reaction results in its consumption by the reverse of reaction (9). Therefore, during overcharge, two reactions occur on the negative, namely, MH charging and oxygen reduction. The potential of the system is therefore a mixed potential, which depends on the fraction of the current going to each reaction. When the cell temperature increases (i.e. isothermal to adiabatic charge), the i_0 of the oxygen reduction reaction increases, which in turn results in the overpotential for this reaction decreasing. This decrease in the overpotential results in the potential of the negative electrode shifting to more positive values thereby decreasing the cell potential. This increase in reaction kinetics is the cause for the increased rollover feature, seen in Fig. 8, as the temperature increases.

4.2. Pore-level model

While the macro-homogeneous models provide insights to the behavior of the cell from a macroscopic scale, details on the phenomena on a microscopic scale are lost. In this section, we describe the pore-level models developed in order to capture this effect. We illustrate this using the two different configurations of active material, shown in Fig. 3. We simulate discharge behavior of a carbon electrode where lithium is de-intercalated from the active material. As model geometry 2 has non-reacting binder in addition to active material, the total amount of dischargable material is reduced. This is seen from the concentration profiles of Li in the solid phase 20 min into discharge, shown in Fig. 9. The plot was generated at 1 C rate corresponding to model 1, which is approximately 2 C for model 2. As the volume of active material is less in model 2 compared to model 1, the moles of active material is also less. Hence, after discharge at the same current for the same time, the concentration in model 2 is lower than that in model 1, as seen in the figure. Although considerable concentration variations are seen in the solid phase concentrations in the figure, no such differences are seen in the liquid phase concentration, indicating that under these conditions, liquid phase limitations are negligible. In addition, the differences in the configuration of the active material result in differences in the diffusion flux into the active material between the two models. Note that in these simulations the binder and active material were assumed to be the same electronic conductivity.

The approach shown here is an ideal procedure for evaluating a number of electrode configurations that are

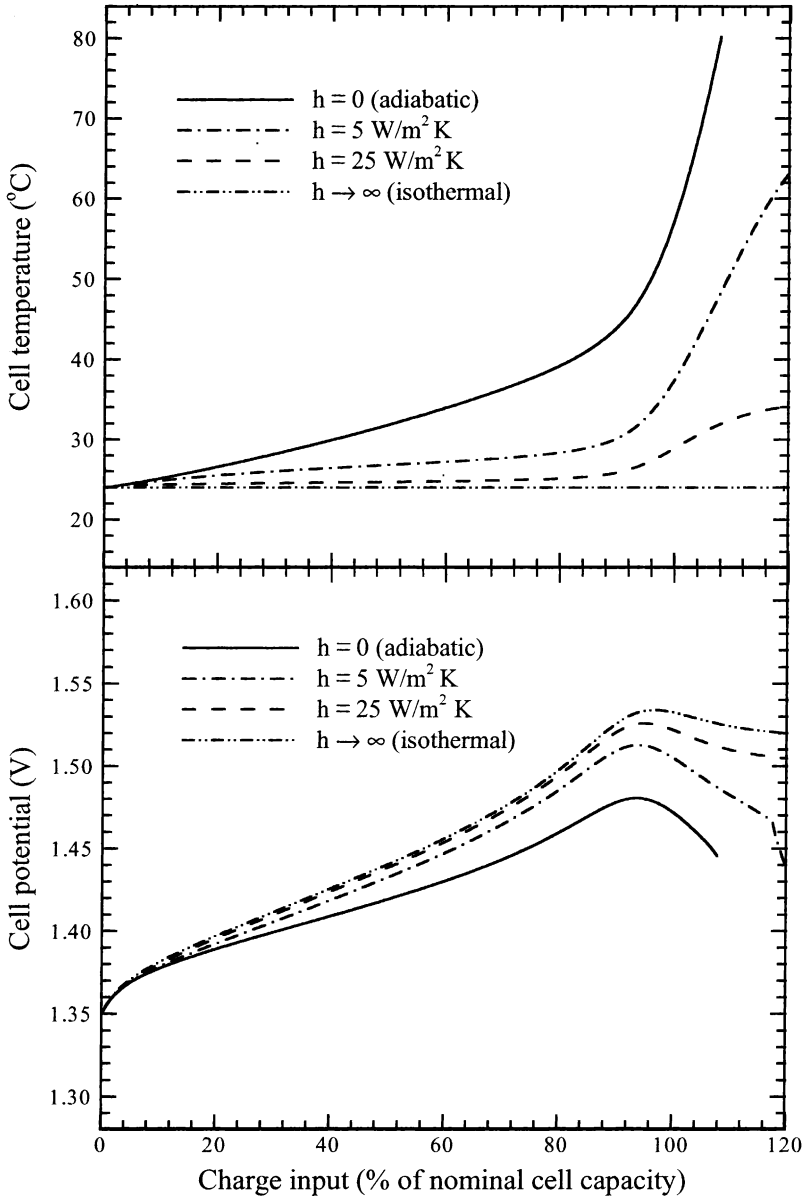

Fig. 8. Temperature (top) and voltage (bottom) vs. charge input for a Ni–MH cell under conditions ranging from isothermal to adiabatic. The graph shows the voltage rollover occurring from oxygen reduction in the MH electrode [8].

impossible to describe using a macro-homogeneous model. These include the ability to study effect of adding conducting binders in less conducting active material, irregularly shaped particles in electrodes, studying particle size distributions as opposed to a bimodal distribution [58,59], and studying the effect of having graded porosity/pore size in the electrode [60]. The DNS technique provides an excellent method of evaluating and testing various electrode configurations prior to electrode manufacture.

4.3. Stack-level model

We finally examine the third level of modeling, namely stack modeling of batteries. Specifically, we are interested in simulating the behavior of cells that are connected with each other in a stack and the SOC balancing issues that arise due to thermal excursions. Consider two Ni–H_2 cells connected together in parallel, with each cell at a different temperature and charged at a constant current to the stack [14]. This can be thought of as two cells at different positions in a cell stack. As the temperatures in the cells are different, the various resistances in the cell are also different, thereby resulting in different characteristics. When the cells are connected externally in parallel, the voltages in the two are forced to be a constant, which then results in differences in the current to each cell, with their sum being a constant. This is seen in Fig. 10, where the total reaction current in the two cells is plotted as the batteries are charged [14]. The graph was made by using two cell-level thermal–electrochemical models and imposing the conditions that the

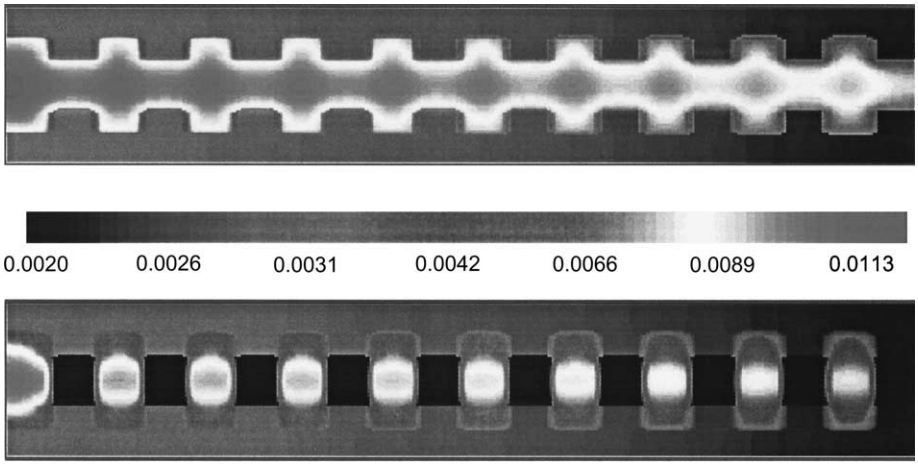

Fig. 9. Concentration (mol/cm^3) contours for lithium in the matrix and solution during discharge of a carbon electrode in a Li-ion cell schematized in Fig. 3. While the concentration in solution refers to Li^+, in the matrix it refers to Li. The top frame refers to model 1 and the bottom frame to model 2.

voltage of the two cells remain the same and that the currents sum up to the external current to the stack.

During charge, Ni oxidation is the primary reaction in the positive electrode, which on overcharges transitions to the oxygen evolution reaction. At low states of charge, the cell with the higher temperature has a lower voltage closer to its equilibrium value, whereby a greater current is passed to the cell in order to make its voltage match that of the cooler cell. As charge continues, the hotter cell reaches full charge faster and hence the current to the cell decreases compared to the colder cell. However, on overcharge, the oxygen evolution reaction starts to occur, which is more energetic for the hotter cell compared to the cooler cell hence resulting in a similar profile as that seen in the first part of the charge. At longer times, the Ni reaction reaches completion in both the cells and only oxygen evolution occurs, which results in the current reaching a steady state. More details can be found in [14].

Fig. 10 is an example of the complex interactions that can occur in a cell stack due to the cross talk between the different cells. In other words, simulation of stack behavior, where interaction between the cells is not considered, would be inaccurate. In addition, Fig. 10 was simulated by holding the temperature of each battery the same through the charge; a condition that is not expected in reality. Efforts are now underway to study cell stacks where in addition to electrochemical variations, temperature variations are also being included. A parallel computer based on PC clusters is used for these calculations. This study, being conducted for Li-ion cells, is expected to generate useful information for development of thermal management systems for cell stacks.

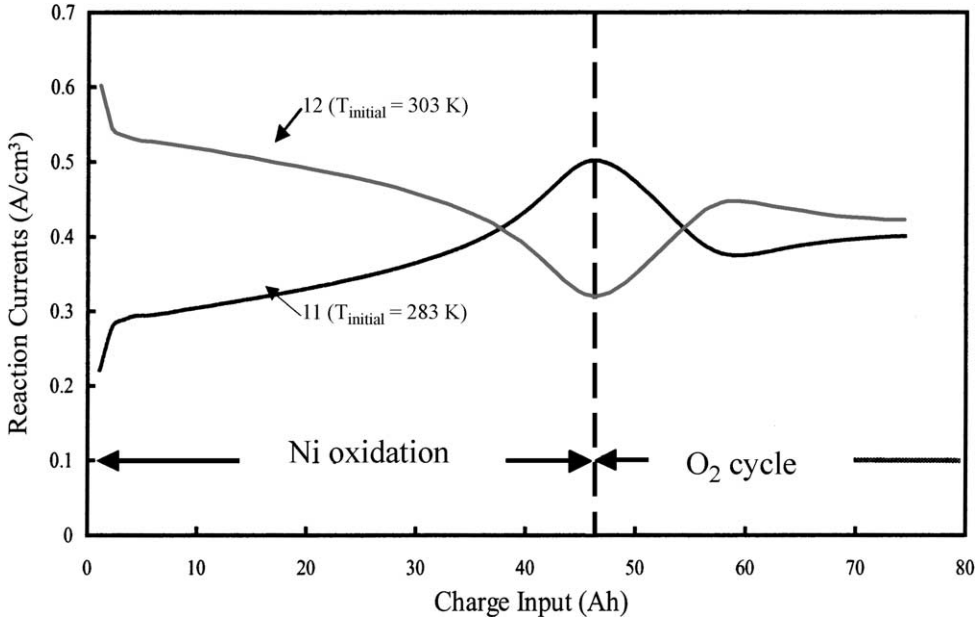

Fig. 10. Reaction current vs. charge input for two Ni–H_2 cells, connected in parallel, one at 283 K and other at 303 K. The graph is simulated during charge when a constant current is passed to the stack [14].

5. Conclusions

This paper reviews the development of a first-principle based mathematical models to describe batteries on a framework parallel to CFD, termed CBD. Specifically two examples of this approach are illustrated, namely, development of thermal–electrochemical coupled models and the development of multi-scale models. The model equations and the significant results from a pore-level, cell-level and stack-level model are reviewed.

The cell-level models are used to show the importance of a combined thermal–electrochemical modeling approach to describe thermal behavior of batteries.

Specifically, experimental data under one condition (e.g. isothermal) cannot be used to predict thermal excursions under other conditions; a problem avoided by the use of an electrochemical model. In addition, the combined experimental/model approach is used to show the ability of the models to describe behavior under different rates using a Ni–MH cell as example. The pore-level models were used to illustrate the ability to simulate complex interfacial geometries, which are ignored in cell-level models. Finally, the ability to simulate cell stacks was illustrated by taking two Ni–H_2 cells at different temperatures, connected in parallel and charged using as a constant current, as an example. The importance of incorporating the interaction between the two batteries in stack simulations is shown.

Acknowledgements

The authors wish to gratefully acknowledge the financial support from DARPA Tactical Technology Office (TTO) under cooperative agreement No. MDA 972-95-2-0009 and 972-95-3-0019, DOE GATE center under cooperative agreement No. DE-FCO2-98CH10954, NSF under grant Nos. DOE-9979579 and CTS-9733662, and NASA/Jet Propulsion Laboratory over the last 5 years. Dr. Wen-Bin Gu developed the Ni-MN and the Li-ion models and Yinghui Pan performed the experimental-model comparison for the Ni–MH cells. Guoqing Wang developed the pore-level models and Rebecca Cullion developed the stack model for the Ni–H_2 cells.

References

[1] J. Newman, Electrochemical Systems, 2nd Edition, Prentice-Hall, Englewood Cliffs, NJ, 1973.
[2] V. Johnson, A. Pesaran, T. Sack, in: Proceedings of the 17th Electric Vehicle Symposium, Montreal, Canada, 2000.
[3] C. O'Gorman, D. Ingersoll, R. Jungst, T. Paez, in: W.R. Cieslak, et al. (Eds.), Selected Battery Topics, Vol. PV 98-15, The Electrochemical Society Proceedings Series, Pennington, NJ, 1998, p. 248.
[4] W.B. Gu, C.Y. Wang, B.Y. Liaw, J. Electrochem. Soc. 144 (1997) 2053.
[5] W.B. Gu, C.Y. Wang, S.M. Li, M.M. Geng, B.Y. Liaw, J. Electrochem. Soc. 44 (1999) 4525.
[6] W.B. Gu, C.Y. Wang, in: S. Surampudi, R.A. Marsh, Z. Ogumi, J. Prakash (Eds.), Proceedings of the Symposium on Lithium Batteries, Vol. 99-25, The Electrochemical Society Proceedings Series, Pennington, NJ, 2000, p. 748.
[7] W.B. Gu, C.Y. Wang, J. Weidner, R. Jungst, G. Nagasubramanian, J. Electrochem. Soc. 147 (2000) 427.
[8] W.B. Gu, C.Y. Wang, J. Electrochem. Soc. 147 (2000) 2910.
[9] C.Y. Wang, W.B. Gu, B.Y. Liaw, J. Electrochem. Soc. 145 (1998) 3407.
[10] C.Y. Wang, W.B. Gu, B.Y. Liaw, J. Electrochem. Soc. 145 (1998) 3418.
[11] S. Um, C.Y. Wang, K.S. Chen, J. Electrochem. Soc. 147 (2000) 4485.
[12] W.B. Gu, C.Y. Wang, B.Y. Liaw, J. Power Sources 71 (1) (1998) 154.
[13] G.Q. Wang, C.Y. Wang, in: The Electrochemical Society Extended Abstracts, Vol. 99-2, The Electrochemical Society Proceedings Series, 1999, p. 212.
[14] R. Cullion, Computational fluid dynamic modeling of a nickel hydrogen battery, Masters Thesis, Pennsylvania State University, University Park, 2000.
[15] J.S. Newman, C.W. Tobias, J. Electrochem. Soc. 109 (1962) 1183.
[16] J.S. Dunning, Analysis of porous electrodes with sparingly soluble reactants, Ph.D. Thesis, University of California, Los Angeles, 1971.
[17] J.A. Trainham, Flow-through porous electrodes, Ph.D. Thesis, University of California, Berkeley, 1979.
[18] J.C. Slattery, Momentum, Energy, and Mass Transfer in Continua, 2nd Edition, Robert E. Krieger Publishing Company, New York, 1981.
[19] P. De Vidts, R.E. White, J. Electrochem. Soc. 144 (1997) 1343.
[20] R. DeLevie, Electrochemical response of rough and porous electrodes, in: C.W. Tobais (Ed.), Advances in Electrochemistry and Electrochemical Engineering, Interscience, New York, 1967.
[21] F.A. Posey, J. Electrochem. Soc. 111 (1964) 1173.
[22] J. Newman, W. Tiedmann, AIChE J. 21 (1975) 25.
[23] J.W. Weidner, Linear-sweep voltammetry at porous electrodes, Ph.D. Thesis, North Carolina State University, Raleigh, 1991.
[24] J. Bouet, F. Richard, P. Blanchard, in: D.A. Corrigan, A.H. Zimmerman (Eds.), Proceedings of the Symposium on Nickel Hydroxide Electrodes, Vol. PV 90-4, The Electrochemical Society Proceedings Series, Pennington, NJ, 1990, p. 260.
[25] P. De Vidts, J. Electrochem. Soc. 142 (1995) 1509.
[26] P. De Vidts, Mathematical modeling of a nickel/hydrogen cell, Ph.D. Thesis, Texas A&M University, College Station, 1995.
[27] P. De Vidts, J. Delgado, R.E. White, J. Electrochem. Soc. 143 (1996) 3223.
[28] P. De Vidts, J. Delgado, B. Wu, D. See, K. Kosanovich, R.E. White, J. Electrochem. Soc. 145 (1998) 3874.
[29] Z. Mao, P. De Vidts, R.E. White, J. Newman, J. Electrochem. Soc. 141 (1994) 54.
[30] J.W. Weidner, P. Timmerman, J. Electrochem. Soc. 141 (1994) 346.
[31] B. Paxton, J. Newman, J. Electrochem. Soc. 144 (1997) 3818.
[32] M. Doyle, T.F. Fuller, J. Newman, J. Electrochem. Soc. 143 (1993) 1526.
[33] M. Özisik, Boundary Value Problems of Heat Conduction, Dover Publications, New York, 1968.
[34] D.N. Bennion, Phenomenon at a gas electrode–electrolyte interface, Ph.D. Thesis, University of California, Berkeley, 1964.
[35] J. Newman, D. Bennion, C.W. Tobais, Berichte der Bunsengesellschaft fur physikalische Chemie 69 (1965) 608.
[36] J. Newman, D. Bennion, C.W. Tobais, Berichte der Bunsengeselischaft fur physikalische Chemie 70 (1966) 493.
[37] J. Newman, T.W. Chapman, AIChE J. 19 (1973) 343.
[38] L. Rao, J. Newman, Electrochem. Soc. 144 (1997) 2697.
[39] J. Newman, Ind. Eng. Chem. Res. 34 (1995) 3208.
[40] N.A. Godshall, J.R. Driscoll, J. Electrochem. Soc. 131 (1984) 2221.
[41] K. Thomas, C. Boguta, J. Newman, J. Electrochem. Soc. 148 (2001) A570.

[42] D. Bernardi, E. Pawlikowski, J. Newman, J. Electrochem. Soc. 132 (1985) 5.
[43] M. Doyle, J. Newman, A.S. Gozdz, C.N. Schmutz, J. Tarascon, J. Electrochem. Soc. 143 (1996) 1890.
[44] Q. Wang, H. Li, X. Huang, L. Chen, J. Electrochem. Soc. 148 (2001) A737.
[45] O. Lanzi, U. Landau, J. Electrochem. Soc. 138 (1991) 2527.
[46] A.S. Viner, P.S. Fedkiw, J. Electrochem. Soc. 137 (1990) 1435.
[47] M. Sahaouri, M. Kaviany, Int. J. Heat Mass Transfer 37 (1994) 2817.
[48] S.V. Patankar, Numerical Heat Transfer and Fluid Flow, Hemisphere, Washington, DC, 1980.
[49] D. Baker, M. Verbrugge, J. Electrochem. Soc. 146 (1999) 2413.
[50] G. Botte, B. Johnson, R. White, J. Electrochem. Soc. 146 (1999) 914.
[51] S. Al Hallaj, R. Venkatachalapathy, J. Prakash, J.R. Selman, J. Electrochem. Soc. 147 (2000) 2432.
[52] T. Fuller, M. Doyle, J. Newman, J. Electrochem. Soc. 141 (1994) 1.
[53] Y. Chen, J. Evans, J. Electrochem. Soc. 143 (1996) 2708.
[54] C. Pals, J. Newman, J. Electrochem. Soc. 142 (1995) 3282.
[55] M. Jam, A.L. Elmore, M.A. Matthews, J.W. Weidner, Electrochim. Acta 43 (18) (1998) 2649.
[56] V. Srinivasan, J.W. Weidner, R. White, J. Solid State Electr. 4 (2000) 367.
[57] V. Srinivasan, J.W. Weidner, J. Newman, J. Electrochem. Soc. 148 (2001) A969.
[58] R. Darling, J. Newman, J. Electrochem. Soc. 144 (1997) 4201.
[59] G.S. Nagarajan, J.W. Van Zee, R.M. Spotnitz, J. Electrochem. Soc. 145 (1998) 771.
[60] Y. Chiang, B. Hellweg, The Electrochemical Society Extended Abstracts, Vol. 2001/2, San Francisco, 2001, p. 144.